Science Advances
AAAS

Supplementary Materials for

Superoxide formation upon photochemical aging of secondary organic aerosols derived from biomass burning precursors

Lena Gerritz *et al.*

Corresponding author: Manabu Shiraiwa, m.shiraiwa@uci.edu

Sci. Adv. **12**, eaeg1621 (2026)
DOI: 10.1126/sciadv.aeg1621

This PDF file includes:

Additional Experiments: Temperature and Concentration Dependence

The concentration of dissolved oxygen is temperature dependent, as shown by the red trace of Fig. S3. By measuring the concentration of BMPO(OOH) in α-pinene SOA aliquots taken at different temperatures, we isolated the influence of dissolved oxygen concentration on BMPO(OOH) formation. After extraction, the SOA was divided and kept at different temperatures: room temperature (~296 K), refrigerated (~ 281 K), and warm water bath (~310 K). After about 20 min of temperature equilibration, 20 mM BMPO was added to each sample and 50 μL aliquots were sealed in capillary tubes for EPR analysis, in triplicate. The temperature of the remaining sample was measured using a calibrated thermocouple after the aliquots were removed. Although this was done as promptly as possible, the samples immediately began equilibrating with the room air, so the temperature values should be treated as approximations and are only intended to illustrate the trend. Fig. S3 shows that as temperature increased and dissolved oxygen concentration decreased, the maximum BMPO(OOH) concentration also decreased. Given the rapid thermal re-equilibration of the bulk solution, it is expected that the sealed aliquots were also at room temperature at the time of analysis. However, the sealed capillary limits gas-liquid partitioning, so the oxygen solubility in the solution will reflect the temperature at the time when the aliquot was sealed, despite reaching thermal equilibrium. This was supported by the reproducibility of replicate measurements because the sealed capillary tubes were kept at room temperature while the replicates were run (max 30 min). We did not observe any influence from the temperature of sealed sample on BMPO(OOH) yield, consistent with dissolved oxygen not re-equilibrating in the sealed environment.

We also measured BMPO(OOH) at different concentrations of α-pinene and phenol SOA (Fig. S2a). The maximum concentration of BMPO(OOH) is similar across all concentrations, which further supports the samples are limited by the concentration of dissolved oxygen. This was further supported by the concentration dependent experiments of pinonic acid and cumene hydroperoxide (Fig. S2b), where all samples reached a similar maximum BMPO(OOH) concentration, except for 1 mM pinonic acid where BMPO(OOH) did not reach it, indicating dissolved oxygen was not fully depleted. Based on the results of these experiments, we conducted the rest of our experiments in 1-2 mM extracts of SOA to slow the depletion of dissolved oxygen while remaining above the limit of detection. In summary, these temperature and concentration dependent experiments confirm that the concentration of dissolved oxygen plays a critical role by serving as a precursor for superoxide formation.

Total Peroxide Measurements:

The total aqueous peroxide content for each SOA extract was measured using an iodometric-spectrophotometric method, adapted from the method described by Epstein et al.(*20*) Briefly, upon exposure to peroxides, iodine forms an absorbing I_3^- complex that can be used to detect the total peroxides present in the solution. The I_3^- complex absorbs

most strongly at 362 nm, but the measurements in this experiment were performed at 405 nm to minimize interference from other absorbing species, as previously recommended (*79*). In order to minimize interference from dissolved oxygen, Milli-Q water and glacial acetic acid (ACROS) were purged with N_2 gas for >30 min immediately prior to experimentation. All samples were extracted in purged Milli-Q water. For quantification, a fresh calibration curve was made for each set of experiments by dissolving 30% H_2O_2 in the purged MilliQ water to make standards ranging from 10-500 μM. The final reaction mixtures consisted of 664 μL of aqueous sample or standard solution and 636 μL of purged glacial acetic acid and 700 μL of KI (Fisher Scientific) for a final reaction volume of 2 mL and final [KI] ~5 mM. After the addition of the KI, the reaction vials were capped and sealed to limit dissolved oxygen partitioning and left to react for an hour. For measurement, 200 μL aliquots of each solution were pipetted in triplicate into a 96 well plate and measured using a Promega GloMax Discover microplate reader. Finally, to account for interference from other absorbing species, control experiments were performed for β-ocimene, phenol, guaiacyl acetone, and styrene SOA prepared identically except the KI stock solution was replaced with water.

Kinetic model:

Conditions: We used an initial dissolved oxygen concentration of 0.2 mM in by assuming air with ~20% O_2 and a Henry's law constant of 10^{-3} M atm^{-1} at standard temperature and pressure. Experimental pH of the SOA extracts was unadjusted and fixed at pH= 5 based on the pH of our MilliQ water because the SOA concentrations were too low to affect overall solution pH. The initial concentration of SOA in the model was set to 1 mM and 0.45 mM to reflect the concentrations used in the EPR and H_2O_2 experiments, respectively. The models for all EPR experiments also included 20 mM BMPO while the model simulations for H_2O_2 and ambient droplets did not. When modeling the EPR experiments, we assumed a closed system with O_2 depletion, based on the experiments described above. When modeling the H_2O_2 experiments and extrapolating our model to ambient conditions we fixed the concentration of O_2 to be constant at 0.2 mM because the systems are open to air and able to re-equilibrate based on Henry's Law. Production rates in Fig. 4B were calculated by introducing an additional equation that tracked the concentration in the absence of loss processes, without altering the underlying chemical mechanism. The production rate was then obtained by dividing this concentration by the elapsed reaction time.

Carbonyl and hydroperoxide photolysis: The bounds for carbonyl and peroxide photolysis rate constants were estimated using previously reported absorption cross sections and our lamp flux (*76*). The upper bound (5×10^{-3} s^{-1}) for carbonyl photolysis was calculated using a cross section of 1×10^{-19} cm^2 $molec^{-1}$ from 280-330 nm, the maximum cross section measured for saturated carbonyls, and the lower bound (5×10^{-6} s^{-1}) was estimated using a cross section of 1×10^{-22} cm^2 $molec^{-1}$ (*80*). The upper bound (10^{-3} s^{-1}) for organic hydroperoxide photolysis was estimated using an absorption cross section of 1×10^{-19} cm^2

molec^{-1} from 280 - 300 nm, 1×10^{-20} cm^2 molec^{-1}from 300 - 320 nm, and 1×10^{-21} cm^2 molec^{-1}from 320 - 380 nm and the lower bound (5×10^{-6} s^{-1}) was estimated using a constant cross section of 1×10^{-22} cm^2 molec^{-1} from 280-380 nm (*81*, *82*).

Carbonyl, photosensitizer, and secondary alcohol fraction estimations: α-pinene SOA formed from OH oxidation was found to contain ~50% carbonyl products in the presence of NO and Isoprene+O_3 SOA was found to contain ~70% carbonyl products, but neither of these measurements accurately represent our α-pinene+OH system, so we estimated 40-90% of the products may contain carbonyls (*83*, *84*). α-pinene SOA is colorless, so we do not expect it to contain high concentrations of photosensitizers, so we set the range to be 0.1-30% photosensitizers. Alcohols are a common product of α-pinene SOA so we estimated 30-80% secondary alcohols (*52*). Phenol SOA is less well characterized, so we estimated the range for non-aromatic alcohols and carbonyls to be 1-40% of the products, based on compositional measurements of toluene SOA, and the range of photosensitizers between 1-50% (*83*, *85*).

Total Peroxide estimation: We were unable to glean convincing data for the total peroxide concentration in phenol SOA due to absorption interference, shown in Fig. S19. In the model, we fixed the initial concentration of H_2O_2 at 0.7% based on the assay results (Fig. 2) and the initial concentration of organic peroxides to 0.7% assuming half of them decomposed to produce the H_2O_2, but the model was insensitive to these assumptions. Our assumption is reasonable based on the measurements by Garmash et al. (2020) (*86*) who measured ~2.5% highly oxidized organic molecules (HOMs), which are known to contain peroxides, in chamber generated phenol SOA. For α-pinene SOA, there is a notable difference between the total peroxides and H_2O_2, so we included 0.3% H_2O_2 and 5% initial organic peroxide concentrations.

There are limited quantitative measurements for total peroxide of SOA and significant variation between generation methods, so it is challenging to directly compare these values with literature. Measurements for α-pinene SOA generated in the PSI smog chamber measured ~18% total peroxide after 2 h of irradiation that decreased to 5% after 9 h, however their chamber uses UV-A lights centered at 350 nm, while our lights are UV-B centered at 310 nm. The lower wavelength in our chamber has better overlap with peroxide absorption, so it's reasonable to assume the peroxide content of our samples is lower even after 2 h because they are more readily photolyzed at 310 nm. We previously reported ~50% total peroxide fraction in α-terpineol SOA generated in a potential aerosol mass flow reactor (PAM) (*32*), which is significantly higher than what is observed in this experiment. We believe this discrepancy can be explained by the significant differences in both residence time and OH exposure between environmental and PAM chambers. To our knowledge, there are no previously reported values for total peroxide in β-ocimene or furfural SOA.

MCGA and Sensitivity Studies: We applied the Monte Carlo Genetic Algorithm to fit the experimental data and to determine rate constants (*53*). MCGA allows efficient, automated, and unbiased global optimization of model input parameters by simultaneous fitting to experimental data sets. It allows reliable estimations of unknown rate constants, especially if they are sensitive to the measurements. A limitation of this method is that extensive input parameter sets may not be uniquely determined from limited input data. To address this issue, we have fixed known parameters based on literature values to reduce the number of unconstrained parameters (Table S1). The relative contributions of each photolysis pathway to BMPO(OOH) formation were estimated by setting the initial fraction of photosensitizers, carbonyls, and peroxides to zero and investigating each reactant individually (Fig. S15). Insensitive reactions appropriately labelled in Table S1 were found to have little effect on the BMPO(OOH), BMPO(R), and H_2O_2 fits. The fits were also insensitive to several other reactions above or below a certain order of magnitude. In these cases, the upper or lower limit for the rate constant is specified in Table S1.

Los Angeles Equivalent Aging:

To account for differences between our lamp intensity and solar irradiation affecting photolysis rates, we estimated that 1 min of lamp irradiation is equivalent to approximately 50 min of sunlight. The same lamp was used for all experiments (EPR, H_2O_2, UV-Vis, MS) at the same distance to ensure similar lamp flux, although H_2O_2 and MS samples were irradiated open to air so dissolved O_2 does not deplete. Using the measured lamp flux and calculated Los Angeles solstice solar flux previously reported (*32*), we calculated the flux for UVB (280 -315 nm), UVA (315 - 400 nm), and visible (400 - 700 nm) ranges. Our lamp intensity was ~54, 14, and 4 times larger than the Los Angeles flux for UVB, UVA, and visible light, respectively. Because carbonyls and peroxides both primarily absorb in the UVB wavelength range, we used a factor of 50 to convert between experimental irradiation time and atmospheric aging time. This likely overestimates the equivalent atmospheric aging time due to absorption of species in the UVA and visible regions, especially in phenol SOA which is known to weakly absorb in the near-UV and visible leading to its pale brown color. To account for the uncertainty in atmospheric aging equivalence and aerosol lifetime, Fig. 4 shows the range of ROS concentrations predicted between 1 and 24 h of estimated atmospheric aging.

UV-Visible Absorption Spectroscopy:

To confirm the burst of superoxide was not limited by the depletion of chromophores, UV-Visible spectrophotometry (Shimadzu UV-1800) was used to record absorption spectra of 1 mM α-pinene SOA and 1 mM phenol SOA over the course of irradiation. Briefly, the extracts were placed in a quartz cuvette and sealed using parafilm to mimic the closed environment of the EPR spectroscopy and a dark UV-Vis spectrum was acquired. The samples were then irradiated through the side of the cuvette using the same 100 W Hg lamp at a distance of ~2.5 cm from the light guide, approximately the

same distance from the light guide to the sample in the EPR cavity. The absorption spectra were taken after 1, 2, 5, 10, 20, and 30 min of irradiation. As shown in Fig. S20-S21, the absorption coefficients of both types of SOA changed by less than 10% over the course of the irradiation. This suggests that the observed reduction in the rate of BMPO(OOH) formation (Fig. 1) is not due to the depletion of light-absorbing species in SOA.

Mass transfer rate:

We conducted analysis of mass transfer kinetics of species into and out of droplets to help assess the role of the photolysis-driven free radical production. The net mass transfer rate of a species from the gas to particle phase (J, in $cm^{-3}\ s^{-1}$) can be described as follows (*87*):

$$J = k_{gp}\left(c_g - c_{eq}\right) \quad (1)$$

where c_g (in cm^{-3}) is gas-phase concentration and c_{eq} (in cm^{-3}) is equilibrium concentration or gas-phase concentration right at the surface. The first-order gas–particle mass transfer coefficient (k_{gp}, s^{-1}) can be calculated as (*88*):

$$k_{gp} = 4\pi D_g r_p N_p \beta \quad (2)$$

where D_g ($cm^2\ s^{-1}$) is the gas-phase diffusion coefficient of a species, r_p (cm) is the radius of a particle, N_p (cm^{-3}) is the number of particles per cubic centimeter of air and β is the Fuchs-Sutugin correction factor defined as:

$$\beta = \frac{0.75\alpha(1+Kn)}{Kn^2+Kn+0.283Kn\alpha+0.75\alpha} \quad (3)$$

where α is the mass accommodation coefficient and Kn is the Knudsen number ($Kn=3D_g/\omega r_p$) and ω ($cm\ s^{-1}$) is the mean thermal velocity of a molecule.

As indicated from Eq. (1), the mass transport flux depends strongly on concentration gradient and the net flux is zero when the gas and particle phase are in equilibrium ($c_g = c_{eq}$). The maximum mass transfer rate can be estimated by assuming $c_{eq} = 0$ and the maximum production rate in particles (P, $cm^{-3}\ s^{-1}$) can be calculated by accounting for particle volume concentration as:

$$P = \frac{k_{gp}c_g}{V_p N_p} = \frac{4\pi D_g r_p \beta c_g}{V_p} \quad (4)$$

where V_p (cm^3) is the volume of one particle and N_p (cm^{-3}) is particle number concentration in air.

With the values of $D_g = 0.23\ cm^2\ s^{-1}$ for OH, $D_g = 0.16\ cm^2\ s^{-1}$ for HO_2 and $D_g = 0.15\ cm^2\ s^{-1}$ for H_2O_2, $\alpha = 1$, and $r_p = 500$ nm, P was calculated as $3.9\times10^{-8} – 3.9\times10^{-6}\ M\ s^{-1}$ for OH with $[OH]_g = 0.004 – 0.4$ ppt, $2.0\times10^{-7} – 2.9\times10^{-4}\ M\ s^{-1}$ for HO_2 with $[HO_2]_g = 0.03 – 43$ ppt, and $6.4\times10^{-5} – 3.8\times10^{-2}\ M\ s^{-1}$ for H_2O_2 with $[H_2O_2]_g = 0.01 – 6$ ppb. These values indicate that maximum mass transfer rates are much larger than ROS production rates by photolysis (Fig. 4); however, please note that it is atmospherically unrealistic to assume

equilibrium concentrations as zero. The timescale to reach equilibrium based on mass transfer can be estimated as

$$\tau = \frac{1}{k_{\mathrm{gp}}} \quad (5)$$

With typical N_{p} of 100-1000 cm^{-3}, this timescale is on the order of seconds and within a few minutes. This analysis indicates that mass transfer is relatively fast and it is reasonable to assume that gas-particle equilibrium is established, with photoirradiation shifting the steady state concentrations by producing more ROS in the condensed phase. Once additional ROS is generated by photolysis, there is sufficient time for reactive ROS (e.g., OH, superoxide) to react in the condensed phase before being transported to the gas phase and less reactive ROS (e.g., H_2O_2) could be transported to the gas phase within a few minutes.

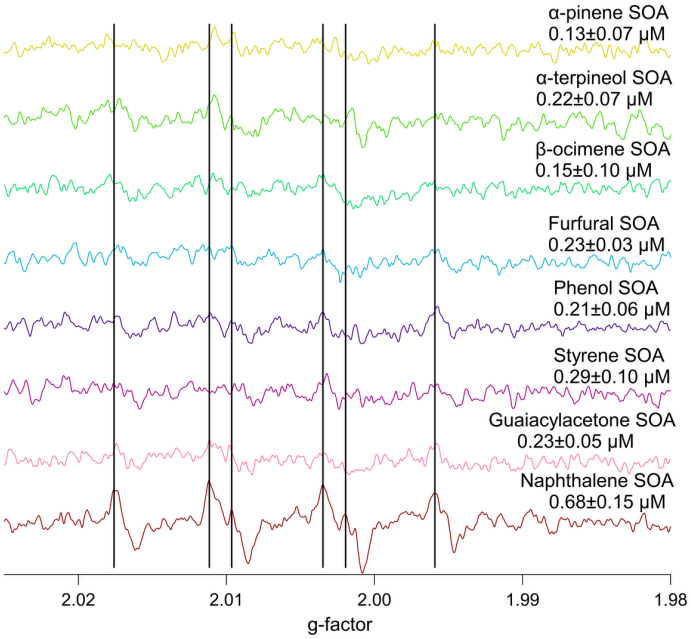

Figure S1: EPR spectra (before irradiation) for each type of 1 mM SOA extract under dark conditions. Vertical lines correspond to BMPO(OOH) peaks observed in naphthalene SOA. Note that the quantified values for all SOA except naphthalene are very close to the limit of detection. For reference, the EPR signal after 10 min of irradiation for α-pinene, furfural, and phenol SOA is shown in Fig. S4.

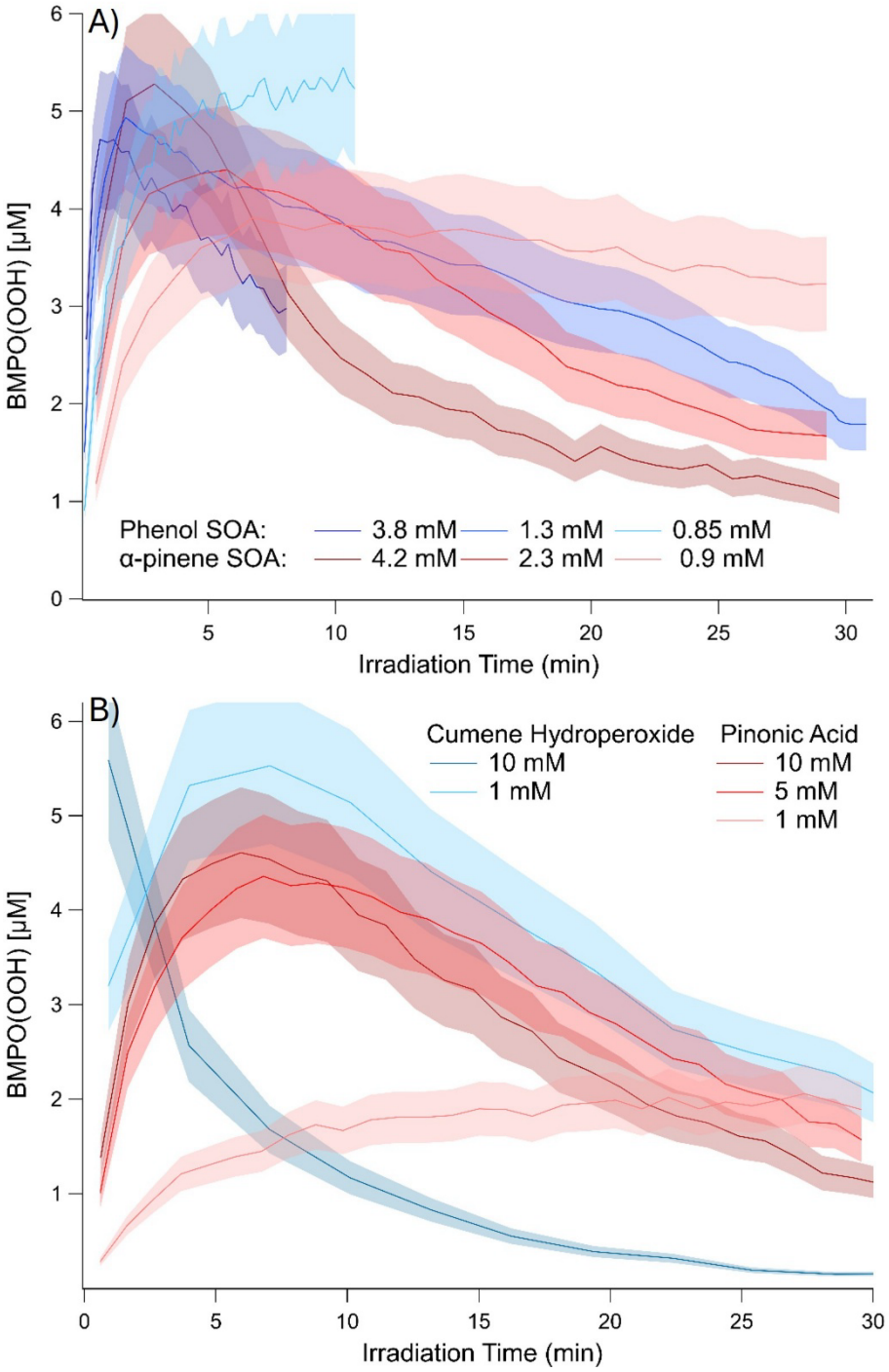

Figure S2: Concentration dependent formation of BMPO(OOH) upon irradiation of A.) α-pinene and phenol SOA and B.) pinonic acid and cumene hydroperoxide standards.

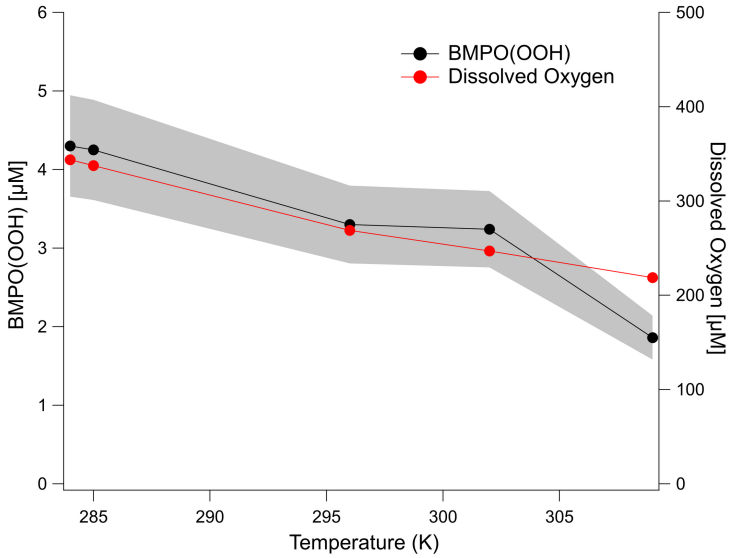

Figure S3: Temperature dependence of the maximum concentrations of BMPO(OOH) reached in irradiated α-pinene SOA and correlation with predicted dissolved oxygen concentrations.

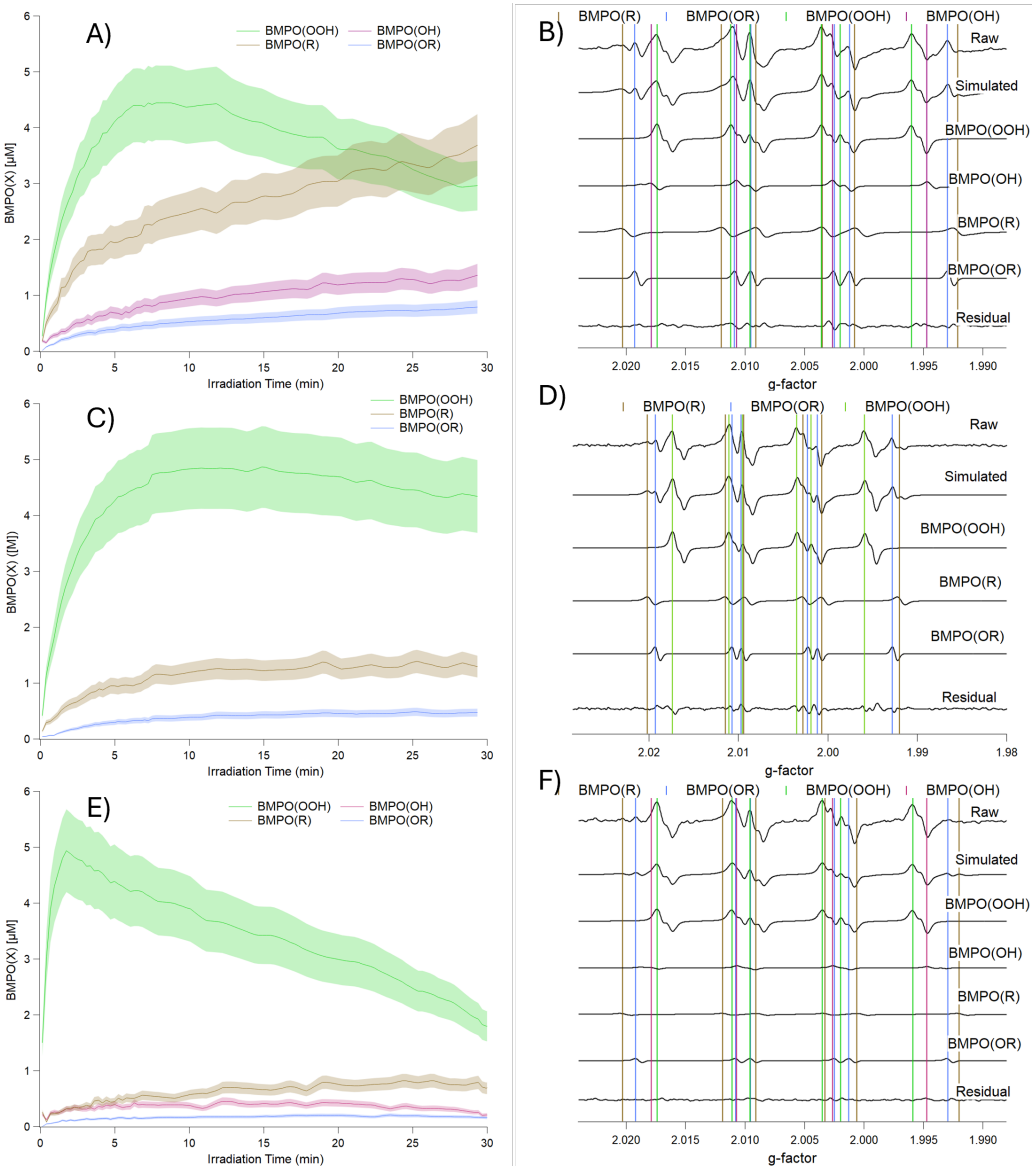

Figure S4: EPR data showing radical formation upon irradiation of ~1 mM A-B) α-pinene SOA, C-D) furfural SOA, E-F) phenol SOA. Panels A, C, E show radical formation over time for each type of SOA. The shading represents 15% error in the measurement, an upper bound for one standard deviation of the measurements. Panels B, D, F show the deconvoluted version of a sample EPR spectra after 10 min of irradiation for each type of SOA.

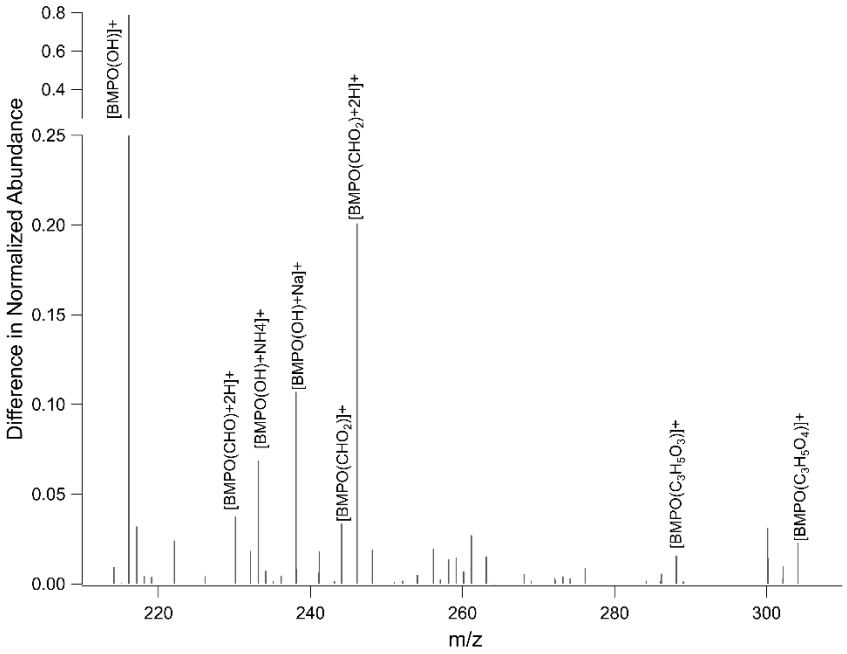

Figure S5: Integrated mass spectrum showing peaks formed during irradiation of furfural SOA based on the difference in normalized abundance of the furfural SOA sample with BMPO before and after irradiation. Labels of major peaks indicate the predicted BMPO adducts based on *m/z*, retention time, and fragmentation patterns (when available).

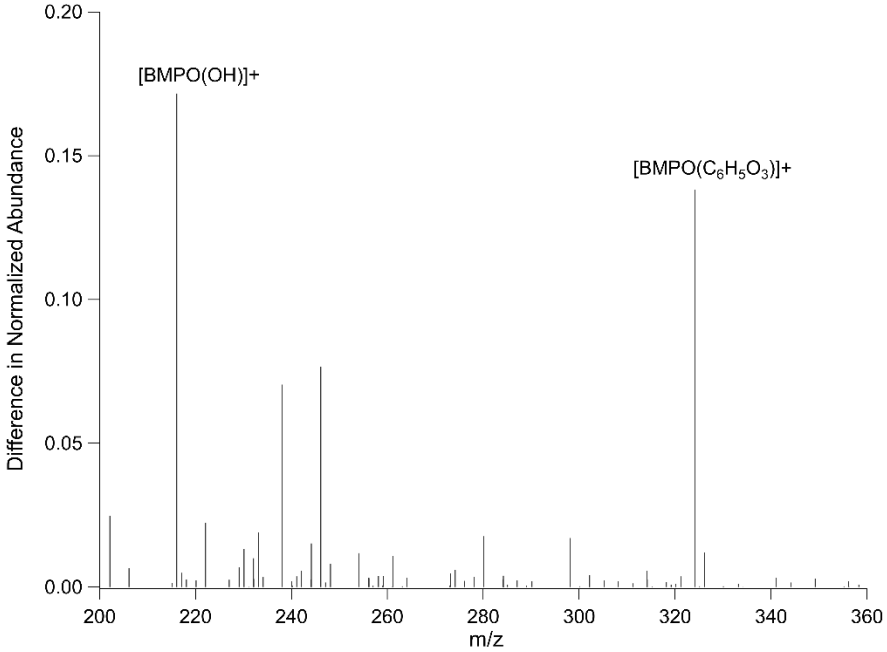

Figure S6: Integrated mass spectrum showing peaks formed during irradiation of phenol SOA based on the difference in normalized abundance of the phenol SOA sample with BMPO before and after irradiation. Labels of major peaks indicate the predicted BMPO adducts based on *m/z* and retention time.

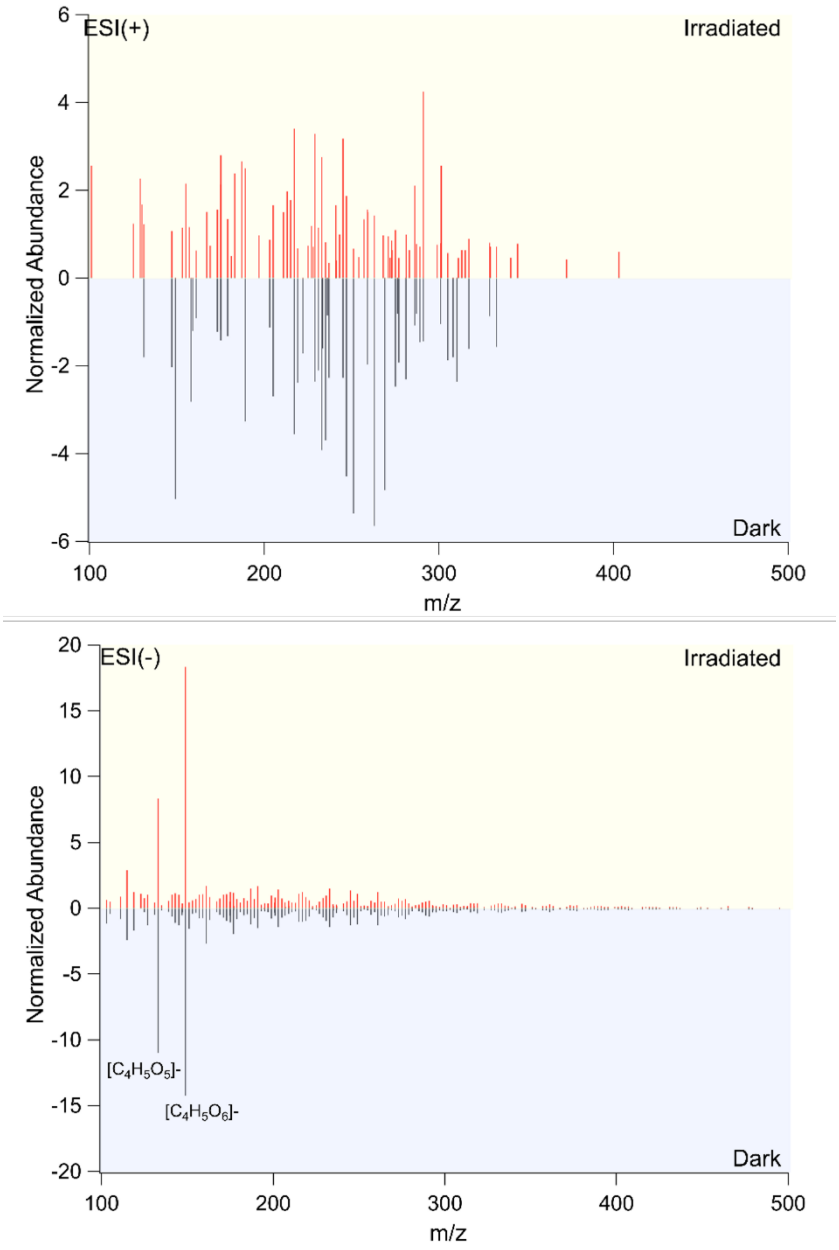

Figure S7: Integrated mass spectra of furfural SOA before and after irradiation in positive and negative ESI. The largest peaks in negative ion mode at *m/z* 133.014 and 149.009 are labeled with their predicted formula.

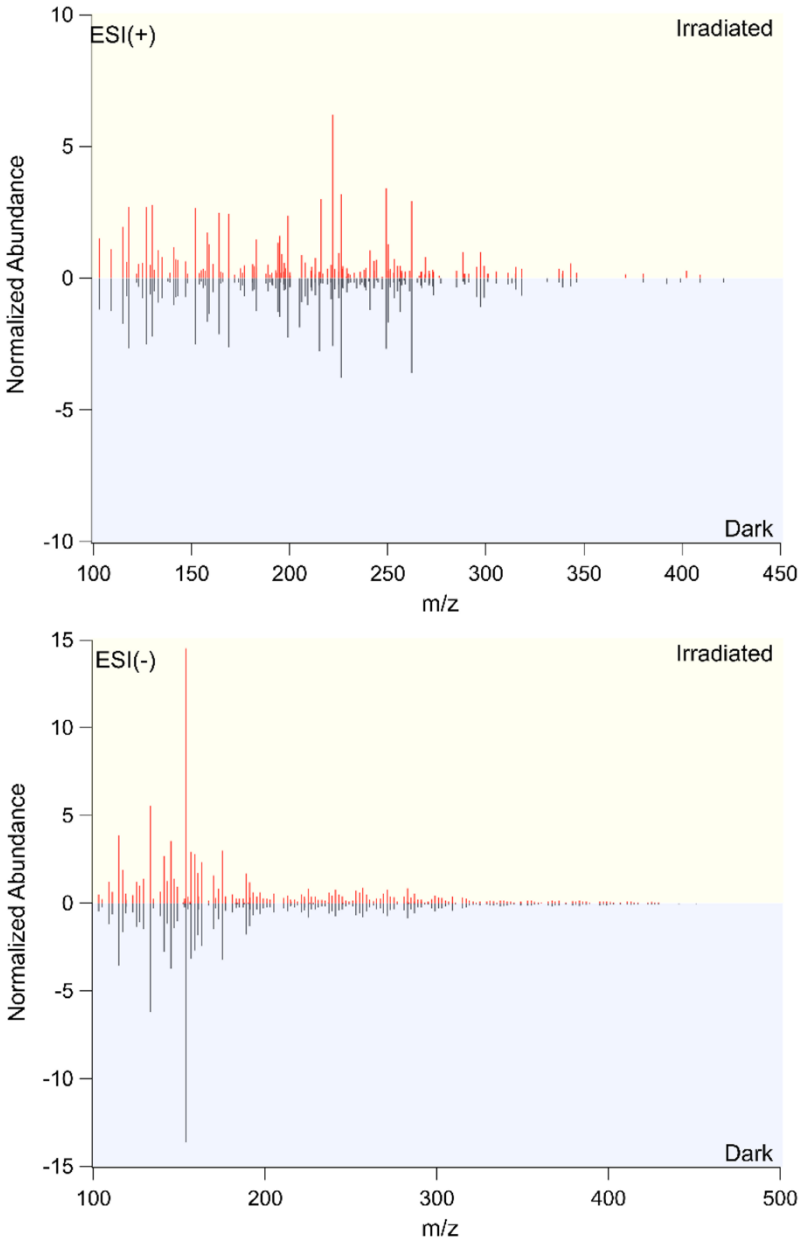

Figure S8: Integrated mass spectra of phenol SOA before and after irradiation in positive and negative ESI.

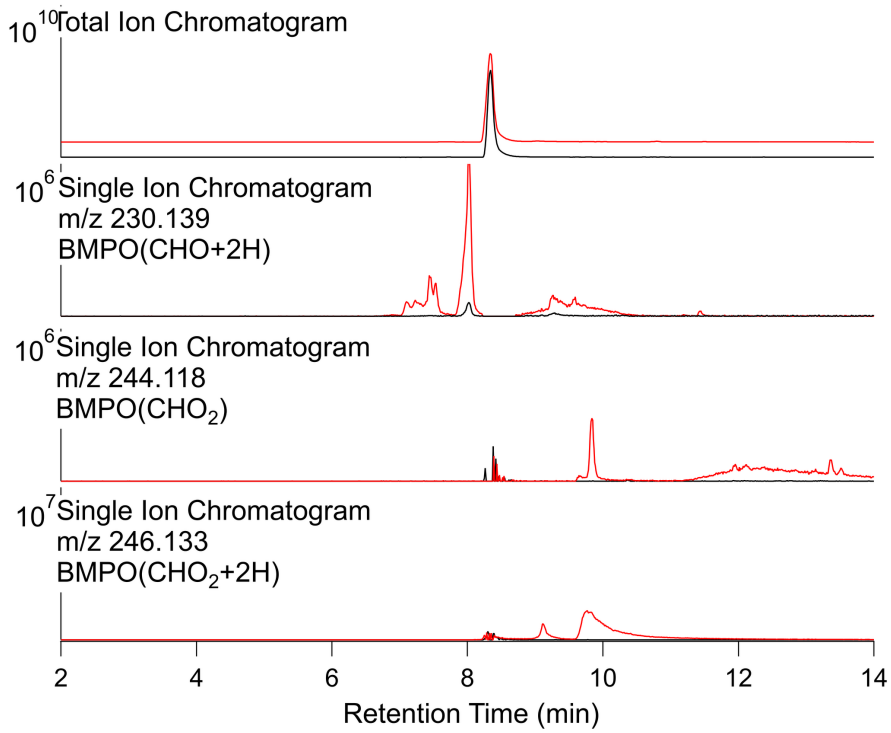

Figure S9: Total ion chromatogram (ESI+) of furfural SOA with BMPO before and after irradiation and single ion chromatograms for major adducts identified in Fig. S5.

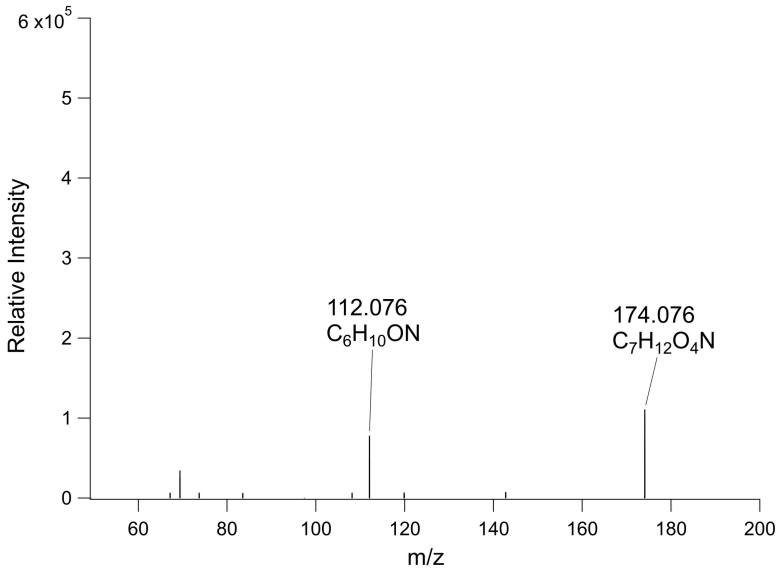

Figure S10: Fragmentation mass spectrum (ESI+) for *m/z* 230.139 in furfural SOA + BMPO. The peak at *m/z* 174.076 is the expected product after losing the t-butyl group from BMPO followed by the loss of CO_2 and H_2O to produce the peak observed at *m/z* 112.076. This is consistent with the fragmentation pattern of a reduced BMPO(CHO) adduct, as previously described (*41*).

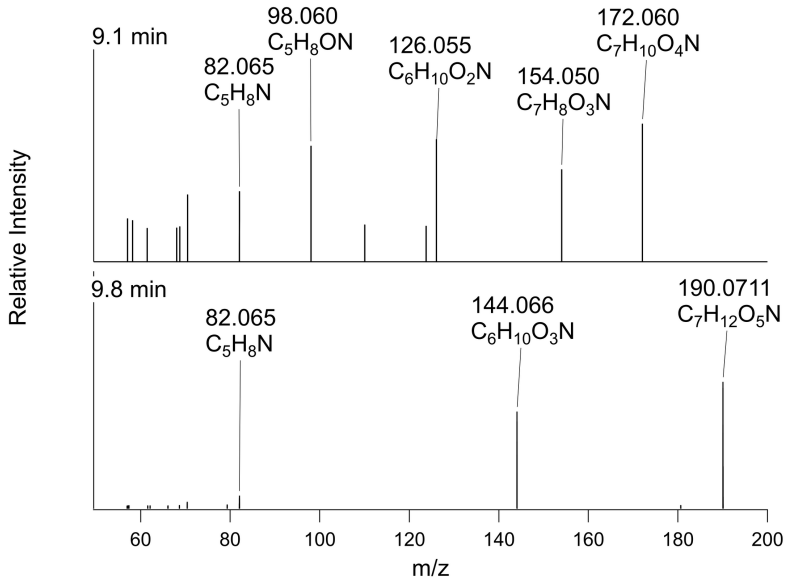

Figure S11: Fragmentation mass spectrum (ESI+) for *m/z* 246.133 at RT 9.1 and 9.8 min in furfural SOA + BMPO. The final peak at *m/z* 82.065 indicates the loss of all functional groups from a reduced BMPO(CHO_2).

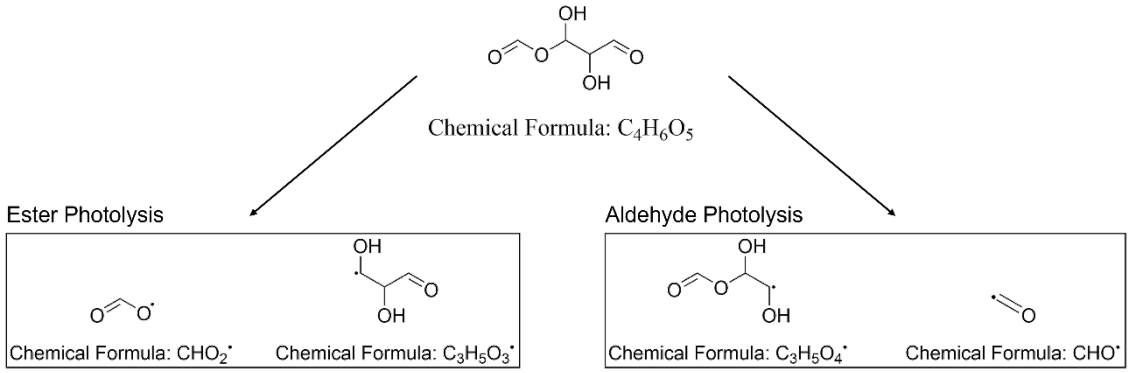

Figure S12: Proposed photolysis mechanism for furfural SOA product $C_4H_6O_5$, using a structure predicted by the GECKO-A model *(89)*. Cleavage of ester and aldehyde functional groups could produce CHO_2· + $C_3H_5O_3$· radicals and CHO + $C_3H_5O_4$ radicals, respectively, corresponding to the major radical adducts identified in Fig. S5.

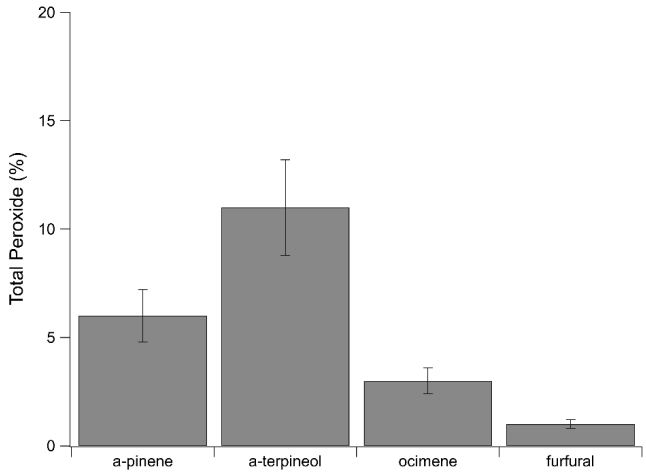

Fig S13: Total peroxide percent fractions measured using the KI absorbance assay for α-pinene, α-terpineol, ocimene, and furfural SOA. Error bars represent 20% deviation based on the upper bound for one standard deviation of replicate measurements.

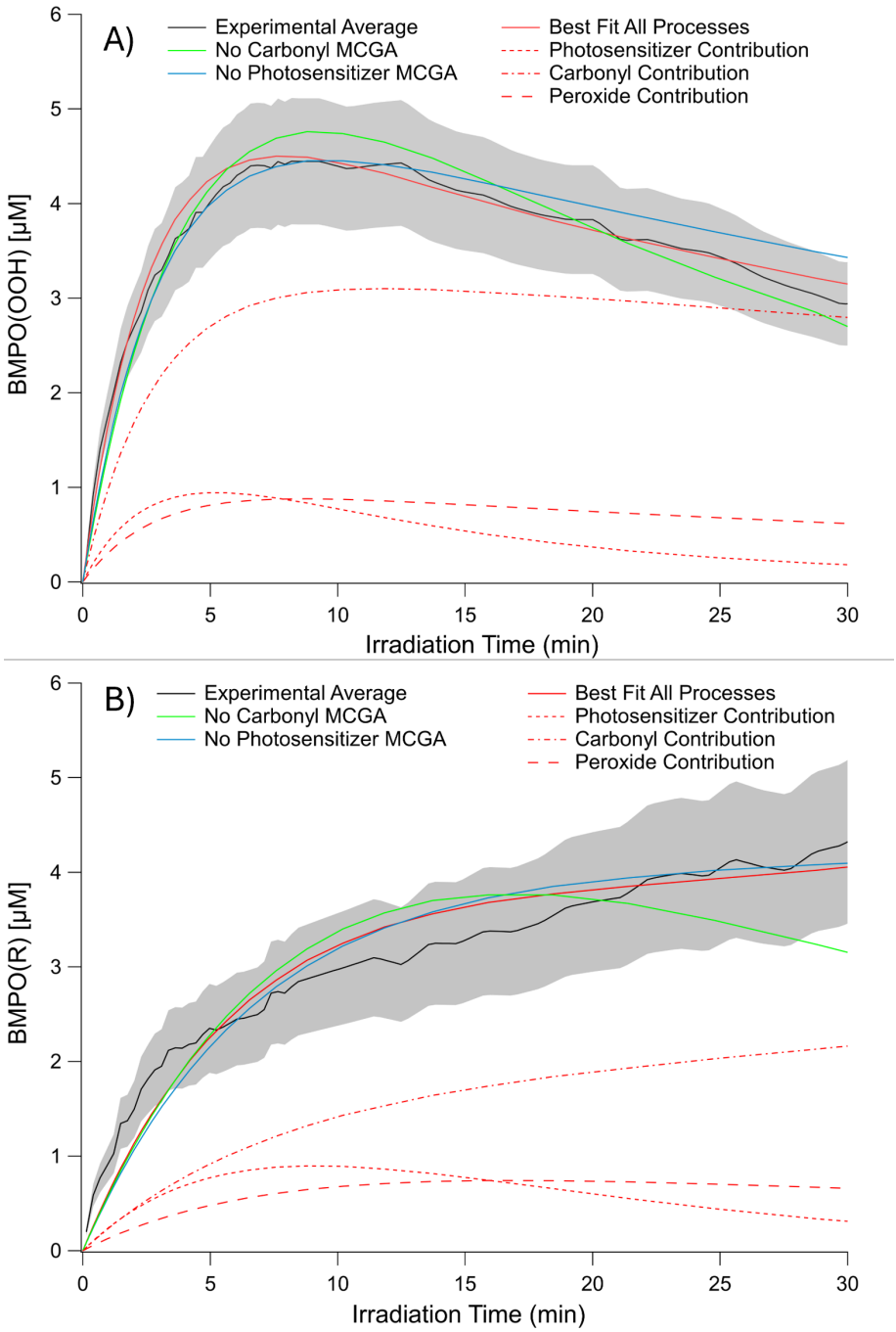

Fig. S14: Model predictions for different photolysis pathways in α-pinene SOA to the formation of A.) BMPO(OOH) and B.) BMPO(R) measured experimentally using EPR (black). The red traces indicate the contributions of each pathway (photosensitizer, carbonyl, peroxide) to the best fit MCGA parameters. The green and blue traces are the best fit parameters from separate MCGA runs without carbonyls or photosensitizers, respectively.

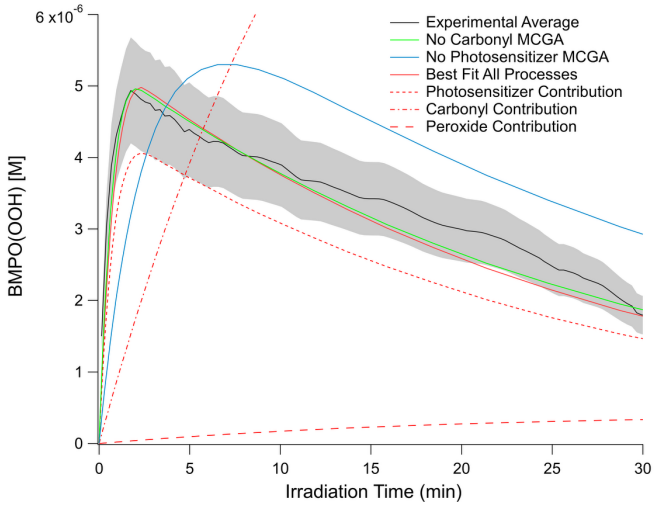

Fig. S15: Model predictions for different photolysis pathways in phenol SOA to the formation of BMPO(OOH) measured experimentally using EPR (black). The red traces indicate the contributions of each pathway (photosensitizer, carbonyl, peroxide) to the best fit MCGA parameters. Note that the predicted carbonyl contribution exceeds the best fit BMPO(OOH) because without the photosensitizers dissolved oxygen depletion is significantly slower (Fig. S16), but this pathway is too slow to compete with the photosensitized reaction in the full system. The green and blue traces are the best fit parameters from separate MCGA runs containing only carbonyls or only photosensitizers.

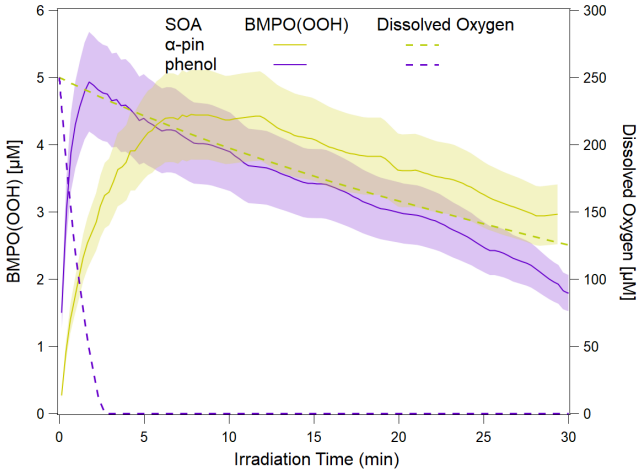

Fig. S16: EPR measured BMPO(OOH) formation (solid lines) and model predicted concentrations of dissolved oxygen (dashed) for 1 mM α-pinene (yellow) and phenol (blue) SOA.

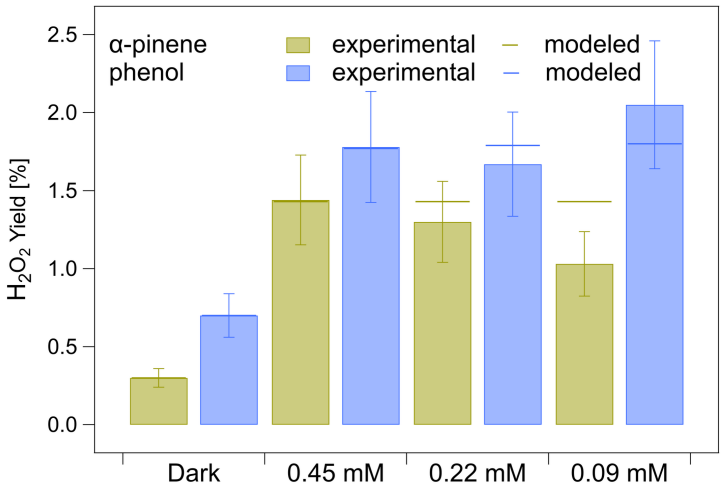

Figure S17: Comparison of experimental H_2O_2 formation and model predictions for α-pinene and phenol SOA before and after 10 min of irradiation at different concentrations.

Error bars represent 20% deviation based on the upper bound for one standard deviation of replicate measurements.

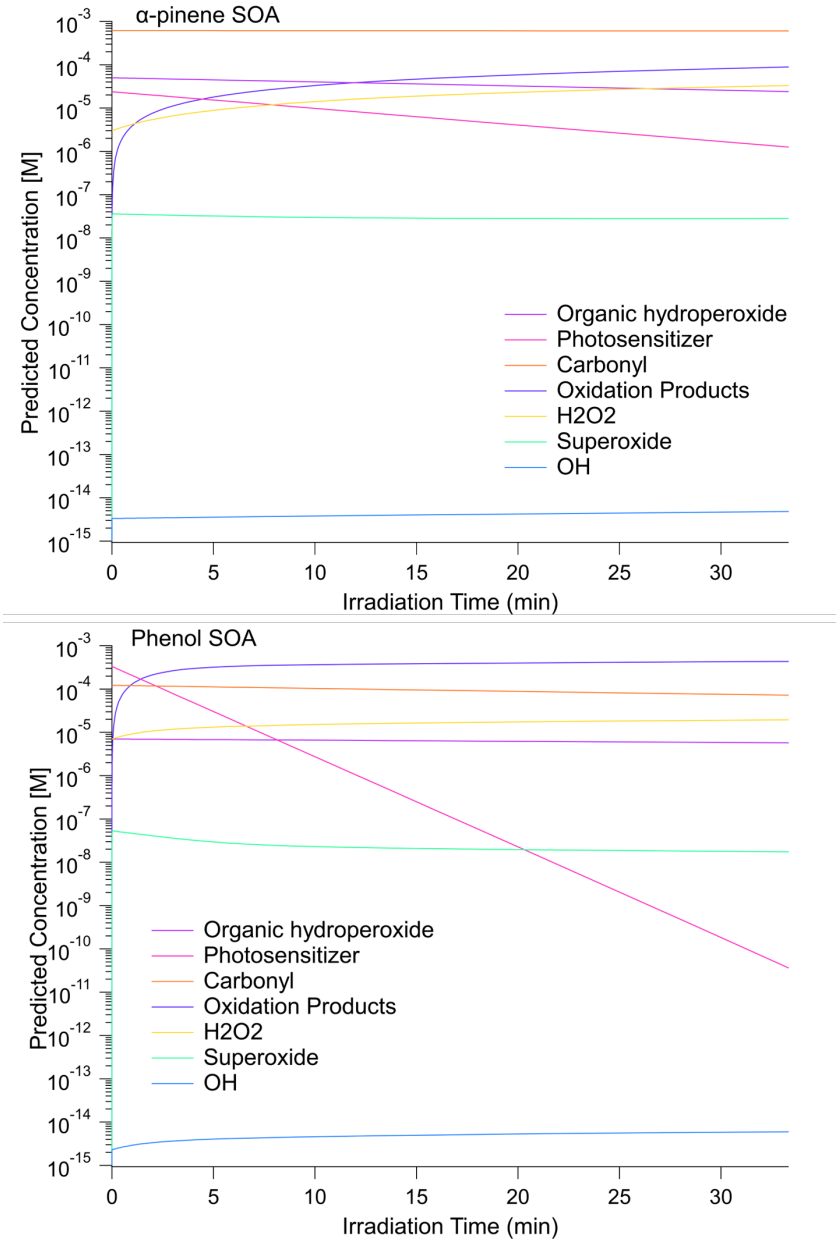

Figure S18: Model predicted evolution of species for 1 mM α-pinene and phenol SOA in systems with constant dissolved oxygen and no BMPO. Oxidation products include the output of reactions 8,33-35.

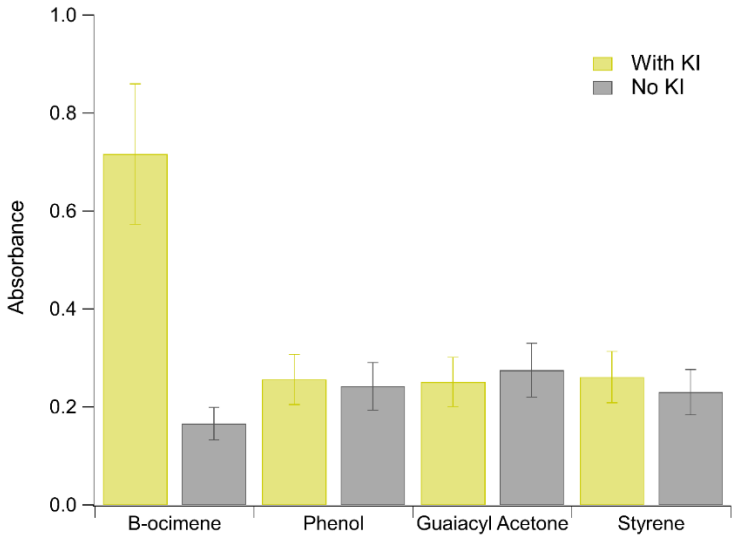

Figure S19: Absorbance at 405 nm for the total peroxide assay both with (yellow) and without (grey) the addition of potassium iodide (KI). Error bars represent 20% deviation based on the upper bound for one standard deviation of replicate measurements.

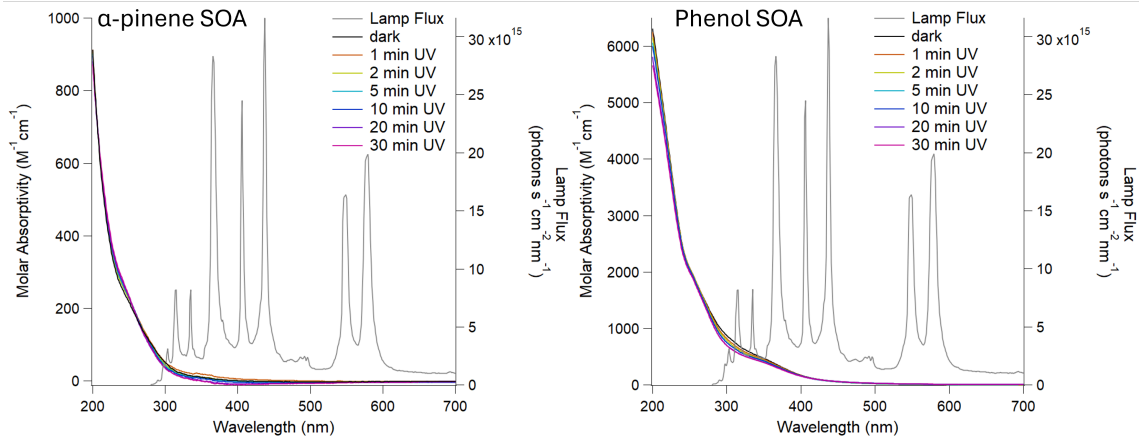

Figure S20: Evolution of the UV-Visible light absorption coefficients for 1 mM α-pinene SOA and phenol SOA over the course of 30 min of irradiation.

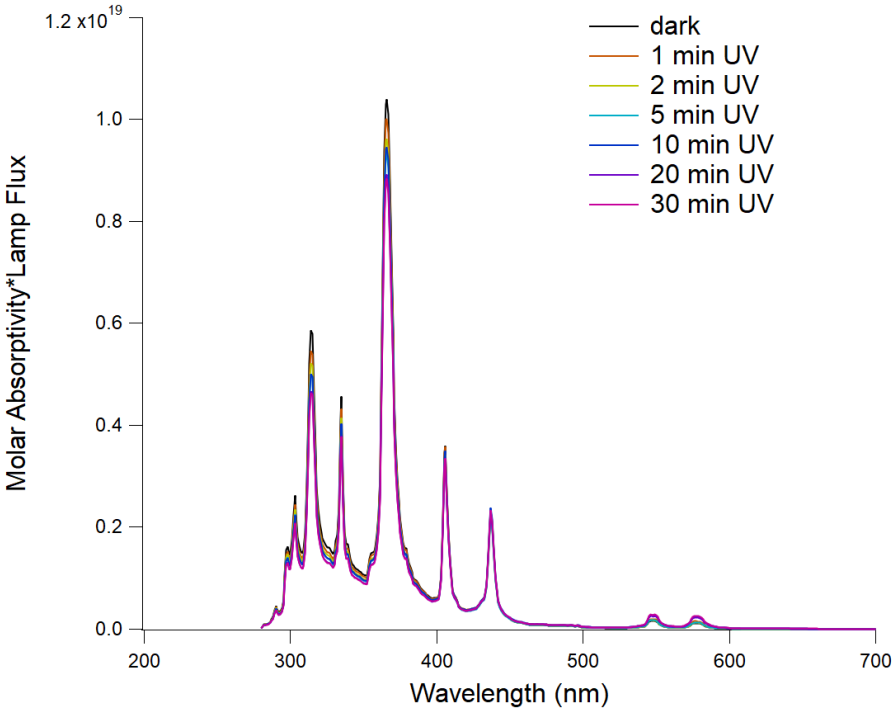

Figure S21: Evolution of the product of molar absorptivity for phenol SOA and the lamp flux over the course of 30 min of irradiation.

Table S1: Rate constant input ranges and best fit rate constants as determined by the application of Monte Carlo Genetic Algorithm (MCGA) to the kinetic model. Rate constants that the overall fits are insensitive to are denoted by an (ẟ). Reactions that are insensitive within certain bounds are labeled (ẟẟ) and the insensitive range is specified.

	Reaction	**Units**	**Best Fit: α-pinene SOA**	**Best Fit: Phenol SOA**	**k source**
	Photosensitization/chromophore reactions				
k_1	PS + hv → PS*	s^{-1}	3.49×10^{-3}	8.59×10^{-3}	(*76*)
k_2	PS*→R•	s^{-1}	1.92×10^{6}	1.1×10^{6}	(*40*)
k_3	PS* + O_2 → PS + $O_2^{-\bullet}$	$M^{-1}s^{-1}$	1.85×10^{9}	1.55×10^{8}	(*40*, *50*)
k_4 ẟẟ (<10^6)	PS + $O_2^{-\bullet}$→ PS*+ O_2	$M^{-1}s^{-1}$	1.00×10^{3}	1.29×10^{3}	
k_5	PS*→PS	s^{-1}	2.20×10^{6}	4.70×10^{4}	(*49*)
	Carbonyl reactions				
k_6	RR'(C=O)+hv→R'(C=O)• + R•	s^{-1}	4.19×10^{-5}	3.10×10^{-4}	See page S3
k_7	R'(C=O)• + O_2→[R'(C=O)O_2•] → HO_2•	$M^{-1}s^{-1}$	3.02×10^{9}	1.39×10^{9}	(*78*)
k_8	R• + O_2 → RO_2•	$M^{-1}s^{-1}$	1.16×10^{9}	4.96×10^{9}	(*78*)
k_9	R•→ products	s^{-1}	1.69×10^{4}	2.24×10^{3}	(*78*)
	Organic hydroperoxide reactions				
k_{10}	ROOH + hv → RO• + HO•	s^{-1}	3.64×10^{-4}	1.00×10^{-4}	See page S3
k_{11}	R_1R_2CHOH + HO• → $R_1R_2C(OH)$•	$M^{-1}s^{-1}$	1.00×10^{10}	1.00×10^{10}	Fixed(*52*)
k_{12} ẟẟ (>10^2)	$R_1R_2C(OH)$•+ O_2 → $R_1R_2C(OH)O_2$•	$M^{-1}s^{-1}$	1.00×10^{10}	1.00×10^{10}	Fixed(*52*)
k_{13} ẟẟ (>1)	$R_1R_2C(OH)O_2$• → $R_1(C=O)R_2$ + HO_2•	s^{-1}	5.00×10^{2}	5.00×10^{2}	Fixed(*52*)
k_{14} ẟ	$R_1R_2C(OH)O_2$•+HO_2• → R(C=O) + H_2O_2	$M^{-1}s^{-1}$	1.00×10^{9}	1.00×10^{9}	(*78*)
	Spin trapping reactions				
k_{15} ẟẟ (>10^5)	BMPO+HO_2• → BMPO(OOH)	$M^{-1}s^{-1}$	1.50×10^{7}	1.50×10^{7}	Fixed(*76*)
k_{16}	BMPO(OOH) → products	s^{-1}	5.91×10^{-3}	6.24×10^{-4}	(*76*, *78*)
k_{17}	BMPO + •OH → BMPO(OH)	$M^{-1}s^{-1}$	5.00×10^{8}	5.00×10^{8}	Fixed(*76*)
k_{18} ẟ	BMPO(OH) → products	s^{-1}	1.65×10^{-3}	1.65×10^{-3}	Fixed(*76*)
k_{19}	BMPO + R• → BMPO(R)	$M^{-1}s^{-1}$	2.26×10^{6}	8.08×10^{2}	(*78*)
k_{20}	BMPO(R) → products	s^{-1}	2.36×10^{-3}	1.48×10^{-4}	(*78*)
	ROS coupling reactions				
k_{21} ẟ	•OH + O_2•$^-$ → O_2 + OH^-	$M^{-1}s^{-1}$	5.97×10^{9}	5.97×10^{9}	Fixed(*76*)
k_{22} ẟẟ (<10^9)	H_2O_2 + •OH → H_2O + HO_2•	$M^{-1}s^{-1}$	1.68×10^{7}	1.68×10^{7}	Fixed(*76*)
k_{23} ẟ	•OH + •OH → H_2O_2	$M^{-1}s^{-1}$	3.52×10^{3}	3.52×10^{3}	Fixed(*76*)

k_{24}[§]	•OH + HO_2• → H_2O + O_2	$M^{-1}s^{-1}$	8.40×10^{9}	8.40×10^{9}	Fixed(*76*)
k_{25}[§]	HO_2• + HO_2• → H_2O_2 + O_2	$M^{-1}s^{-1}$	8.43×10^{5}	8.43×10^{5}	Fixed(*76*)
k_{26}[§§] (<10^7)	H_2O_2 + HO_2• → H_2O + O_2 + •OH	$M^{-1}s^{-1}$	3.00	3.00	Fixed(*76*)
k_{27}[§]	HO_2•+ O_2•$^-$ → H_2O_2 + OH^- + O_2	$M^{-1}s^{-1}$	1.00×10^{8}	1.00×10^{8}	Fixed(*76*)
k_{28}[§§] (>10^7)	H^+ + O_2•$^-$ → HO_2•	$M^{-1}s^{-1}$	6.00×10^{9}	6.00×10^{9}	Fixed(*76*)
k_{29}[§§] (<10^8)	HO_2• → H^+ + O_2•$^-$	s^{-1}	2.30×10^{5}	2.30×10^{5}	Fixed(*76*)
k_{30}	H_2O_2 + *hv* → •OH + •OH	s^{-1}	2.70×10^{-4}	2.70×10^{-4}	Fixed(*76*)
	Miscellaneous organic reactions				
k_{31}[§§] (>1)	RO• →R•	s^{-1}	1.00×10^{6}	1.00×10^{6}	Fixed(*78*)
k_{32}	R(C=O)• →R•	s^{-1}	4.77×10^{5}	5.19×10^{5}	(*78*)
k_{33}[§]	RO• + RO• → ROOR	$M^{-1}s^{-1}$	1.00×10^{6}	1.00×10^{6}	Fixed(*78*)
k_{34}[§]	RO• + HO• → ROOH	$M^{-1}s^{-1}$	1.00×10^{9}	1.00×10^{9}	Fixed(*78*)
k_{35}	SOA + HO• → products	$M^{-1}s^{-1}$	1.00×10^{9}	1.00×10^{9}	Fixed(*78*)
	Photosensitizer fraction		0.02	0.33	See page S3
	Carbonyl fraction		0.62	0.12	See page S3
	Alcohol fraction		0.50	0.09	See page S3
	Organic peroxide		0.05	0.007	See page S3
	H_2O_2		0.003	0.007	measured
	Dissolved oxygen [M] (EPR experiments)		2.50×10^{-4} (initial)	2.50×10^{-4} (initial)	See page S3
	Dissolved oxygen [M] (H_2O_2 experiments)		2.50×10^{-4} (constant)	2.50×10^{-4} (constant)	
	SOA [M] (EPR experiments)		0.001	0.001	measured
	SOA [M] (H_2O_2 experiments)		0.00045	0.00044	
	BMPO [M]		0.02	0.02	measured

REFERENCES

1. U. Pöschl, M. Shiraiwa, Multiphase chemistry at the atmosphere–biosphere interface influencing climate and public health in the anthropocene. *Chem. Rev.* **115**, 4440–4475 (2015).

2. M. Shrivastava, C. D. Cappa, J. Fan, A. H. Goldstein, A. B. Guenther, J. L. Jimenez, C. Kuang, A. Laskin, S. T. Martin, N. L. Ng, T. Petaja, J. R. Pierce, P. J. Rasch, P. Roldin, J. H. Seinfeld, J. Shilling, J. N. Smith, J. A. Thornton, R. Volkamer, J. Wang, D. R. Worsnop, R. A. Zaveri, A. Zelenyuk, Q. Zhang, Recent advances in understanding secondary organic aerosol: Implications for global climate forcing. *Rev. Geophys.* **55**, 509–559 (2017).

3. M. O. Andreae, Emission of trace gases and aerosols from biomass burning – An updated assessment. *Atmos. Chem. Phys.* **19**, 8523–8546 (2019).

4. A. L. Westerling, H. G. Hidalgo, D. R. Cayan, T. W. Swetnam, Warming and earlier spring increase western U.S. forest wildfire activity. *Science* **313**, 940–943 (2006).

5. T. C. Bond, S. J. Doherty, D. W. Fahey, P. M. Forster, T. Berntsen, B. J. DeAngelo, M. G. Flanner, S. Ghan, B. Kärcher, D. Koch, S. Kinne, Y. Kondo, P. K. Quinn, M. C. Sarofim, M. G. Schultz, M. Schulz, C. Venkataraman, H. Zhang, S. Zhang, N. Bellouin, S. K. Guttikunda, P. K. Hopke, M. Z. Jacobson, J. W. Kaiser, Z. Klimont, U. Lohmann, J. P. Schwarz, D. Shindell, T. Storelvmo, S. G. Warren, C. S. Zender, Bounding the role of black carbon in the climate system: A scientific assessment. *J. Geophys. Res. Atmos.* **118**, 5380–5552 (2013).

6. S. K. Akagi, R. J. Yokelson, C. Wiedinmyer, M. J. Alvarado, J. S. Reid, T. Karl, J. D. Crounse, P. O. Wennberg, Emission factors for open and domestic biomass burning for use in atmospheric models. *Atmos. Chem. Phys.* **11**, 4039–4072 (2011).

7. A. L. Hodshire, A. Akherati, M. J. Alvarado, B. Brown-Steiner, S. H. Jathar, J. L. Jimenez, S. M. Kreidenweis, C. R. Lonsdale, T. B. Onasch, A. M. Ortega, J. R. Pierce, Aging effects on biomass burning aerosol mass and composition: A critical review of field and laboratory studies. *Environ. Sci. Technol.* **53**, 10007–10022 (2019).

8. A. T. Ahern, E. S. Robinson, D. S. Tkacik, R. Saleh, L. E. Hatch, K. C. Barsanti, C. E. Stockwell, R. J. Yokelson, A. A. Presto, A. L. Robinson, R. C. Sullivan, N. M. Donahue, Production of secondary organic aerosol during aging of biomass burning smoke From fresh fuels and its relationship to VOC precursors. *JGR Atmospheres* **124**, 3583–3606 (2019).

9. T. Wang, K. Li, D. M. Bell, J. Zhang, T. Cui, M. Surdu, U. Baltensperger, J. G. Slowik, H. Lamkaddam, I. El Haddad, A. S. H. Prevot, Large contribution of in-cloud production of secondary organic aerosol from biomass burning emissions. *Npj Clim Atmos Sci* **7**, 149 (2024).

10. P. Lin, P. K. Aiona, Y. Li, M. Shiraiwa, J. Laskin, S. A. Nizkorodov, A. Laskin, Molecular characterization of brown carbon in biomass burning aerosol particles. *Environ. Sci. Technol.* **50**, 11815–11824 (2016).

11. Y. Rudich, N. M. Donahue, T. F. Mentel, Aging of organic aerosol: Bridging the gap between laboratory and field studies. *Annu. Rev. Phys. Chem.* **58**, 321–352 (2007).

12. G. Stefenelli, J. Jiang, A. Bertrand, E. A. Bruns, S. M. Pieber, U. Baltensperger, N. Marchand, S. Aksoyoglu, A. S. H. Prévôt, J. G. Slowik, I. El Haddad, Secondary organic aerosol formation from smoldering and flaming combustion of biomass: A box model parametrization based on volatility basis set. *Atmos. Chem. Phys.* **19**, 11461–11484 (2019).

13. B. B. Palm, Q. Peng, C. D. Fredrickson, B. H. Lee, L. A. Garofalo, M. A. Pothier, S. M. Kreidenweis, D. K. Farmer, R. P. Pokhrel, Y. Shen, S. M. Murphy, W. Permar, L. Hu, T. L. Campos, S. R. Hall, K. Ullmann, X. Zhang, F. Flocke, E. V. Fischer, J. A. Thornton, Quantification of organic aerosol and brown carbon evolution in fresh wildfire plumes. *Proc. Natl. Acad. Sci. U.S.A.* **117**, 29469–29477 (2020).

14. A. Akherati, Y. He, M. M. Coggon, A. R. Koss, A. L. Hodshire, K. Sekimoto, C. Warneke, J. De Gouw, L. Yee, J. H. Seinfeld, T. B. Onasch, S. C. Herndon, W. B. Knighton, C. D. Cappa, M. J. Kleeman, C. Y. Lim, J. H. Kroll, J. R. Pierce, S. H. Jathar, Oxygenated aromatic compounds are important precursors of secondary organic aerosol in biomass-burning emissions. *Environ. Sci. Technol.* **54**, 8568–8579 (2020).

15. M. K. Schueneman, D. A. Day, Z. Peng, D. Pagonis, O. J. Jenks, J. A. De Gouw, J. L. Jimenez, Secondary organic aerosol formation from the OH oxidation of phenol, catechol, styrene, furfural, and methyl furfural. *ACS Earth Space Chem.* **8**, 1179–1192 (2024).

16. B. Ervens, B. J. Turpin, R. J. Weber, Secondary organic aerosol formation in cloud droplets and aqueous particles (aqSOA): A review of laboratory, field and model studies. *Atmos. Chem. Phys.* **11**, 11069–11102 (2011).

17. K. E. Daumit, A. J. Carrasquillo, R. A. Sugrue, J. H. Kroll, Effects of condensed-phase oxidants on secondary organic aerosol formation. *J. Phys. Chem. A* **120**, 1386–1394 (2016).

18. A. Laskin, J. Laskin, S. A. Nizkorodov, Chemistry of atmospheric brown carbon. *Chem. Rev.* **115**, 4335–4382 (2015).

19. S. A. Mang, D. K. Henricksen, A. P. Bateman, M. P. S. Andersen, D. R. Blake, S. A. Nizkorodov, Contribution of carbonyl photochemistry to aging of atmospheric secondary organic aerosol. *J. Phys. Chem. A* **112**, 8337–8344 (2008).

20. S. A. Epstein, S. L. Blair, S. A. Nizkorodov, Direct photolysis of α-pinene ozonolysis secondary organic aerosol: Effect on particle mass and peroxide content. *Environ. Sci. Technol.* **48**, 11251–11258 (2014).

21. V. J. Baboomian, Y. Gu, S. A. Nizkorodov, Photodegradation of secondary organic aerosols by long-term exposure to solar actinic radiation. *ACS Earth Space Chem.* **4**, 1078–1089 (2020).

22. J. D. Smith, V. Sio, L. Yu, Q. Zhang, C. Anastasio, Secondary organic aerosol production from aqueous reactions of atmospheric phenols with an organic triplet excited state. *Environ. Sci. Technol.* **48**, 1049–1057 (2014).

23. Y. Chen, N. Li, X. Li, Y. Tao, S. Luo, Z. Zhao, S. Ma, H. Huang, Y. Chen, Z. Ye, X. Ge, Secondary organic aerosol formation from ^{3}C*-initiated oxidation of 4-ethylguaiacol in atmospheric aqueous-phase. *Sci. Total Environ.* **723**, 137953 (2020).

24. B. R. Go, Y. J. Li, D. D. Huang, C. K. Chan, Aqueous-phase photoreactions of mixed aromatic carbonyl photosensitizers yield more oxygenated, oxidized, and less light-absorbing secondary organic aerosol (SOA) than single systems. *Environ. Sci. Technol.* **58**, 7924–7936 (2024).

25. S. E. Paulson, P. J. Gallimore, X. M. Kuang, J. R. Chen, M. Kalberer, D. H. Gonzalez, A light-driven burst of hydroxyl radicals dominates oxidation chemistry in newly activated cloud droplets. *Sci. Adv.* **5**, eaav7689 (2019).

26. Y. Wang, H. Kim, S. E. Paulson, Hydrogen peroxide generation from α- and β-pinene and toluene secondary organic aerosols. *Atmos. Environ.* **45**, 3149–3156 (2011).

27. X. Chen, P. K. Hopke, W. P. L. Carter, Secondary organic aerosol from ozonolysis of biogenic volatile organic compounds: Chamber studies of particle and reactive oxygen species formation. *Environ. Sci. Technol.* **45**, 276–282 (2011).

28. W. Y. Tuet, Y. Chen, S. Fok, D. Gao, R. J. Weber, J. A. Champion, N. L. Ng, Chemical and cellular oxidant production induced by naphthalene secondary organic aerosol (SOA): Effect of redox-active metals and photochemical aging. *Sci. Rep.* **7**, 15157 (2017).

29. H. Tong, A. M. Arangio, P. S. J. Lakey, T. Berkemeier, F. Liu, C. J. Kampf, W. H. Brune, U. Pöschl, M. Shiraiwa, Hydroxyl radicals from secondary organic aerosol decomposition in water. *Atmos. Chem. Phys.* **16**, 1761–1771 (2016).

30. J. G. Charrier, C. Anastasio, Rates of hydroxyl radical production from transition metals and quinones in a surrogate lung fluid. *Environ. Sci. Technol.* **49**, 9317–9325 (2015).

31. K. M. Badali, S. Zhou, D. Aljawhary, M. Antiñolo, W. J. Chen, A. Lok, E. Mungall, J. P. S. Wong, R. Zhao, J. P. D. Abbatt, Formation of hydroxyl radicals from photolysis of secondary organic aerosol material. *Atmos. Chem. Phys.* **15**, 7831–7840 (2015).

32. L. Gerritz, J. Wei, T. Fang, C. Wong, A. L. Klodt, S. A. Nizkorodov, M. Shiraiwa, Reactive oxygen species formation and peroxide and carbonyl decomposition in aqueous photolysis of secondary organic aerosols. *Environ. Sci. Technol.* **58**, 4716–4726 (2024).

33. R. Kaur, J. R. Labins, S. S. Helbock, W. Jiang, K. J. Bein, Q. Zhang, C. Anastasio, Photooxidants from brown carbon and other chromophores in illuminated particle extracts. *Atmos. Chem. Phys.* **19**, 6579–6594 (2019).

34. A. Manfrin, S. A. Nizkorodov, K. T. Malecha, G. J. Getzinger, K. McNeill, N. Borduas-Dedekind, Reactive oxygen species production from secondary organic aerosols: The importance of singlet oxygen. *Environ. Sci. Technol.* **53**, 8553–8562 (2019).

35. P. Corral Arroyo, T. Bartels-Rausch, P. A. Alpert, S. Dumas, S. Perrier, C. George, M. Ammann, Particle-phase photosensitized radical production and aerosol aging. *Environ. Sci. Technol.* **52**, 7680–7688 (2018).

36. Z. Liang, L. Zhou, C. K. Chan, Fast generation of peroxides via atmospheric particulate photosensitization. *Sci. Adv.* **11**, eadr8776 (2025).

37. K. C. Edwards, A. L. Klodt, T. Galeazzo, M. Schervish, J. Wei, T. Fang, N. M. Donahue, B. Aumont, S. A. Nizkorodov, M. Shiraiwa, Effects of nitrogen oxides on the production of reactive oxygen species and environmentally persistent free radicals from α-pinene and naphthalene secondary organic aerosols. *J. Phys. Chem. A* **126**, 7361–7372 (2022).

38. L. Khachatryan, E. Vejerano, S. Lomnicki, B. Dellinger, Environmentally persistent free radicals (EPFRs). 1. Generation of reactive oxygen species in aqueous solutions. *Environ. Sci. Technol.* **45**, 8559–8566 (2011).

39. J. Wei, T. Fang, C. Wong, P. S. J. Lakey, S. A. Nizkorodov, M. Shiraiwa, Superoxide formation from aqueous reactions of biogenic secondary organic aerosols. *Environ. Sci. Technol.* **55**, 260–270 (2021).

40. J. Ma, J. Nie, H. Zhou, H. Wang, L. Lian, S. Yan, W. Song, Kinetic consideration of photochemical formation and decay of superoxide radical in dissolved organic matter solutions. *Environ. Sci. Technol.* **54**, 3199–3208 (2020).

41. L. Gerritz, V. Perraud, K. M. Weber, M. Shiraiwa, S. A. Nizkorodov, Application of UHPLC-ESI-MS/MS to identify free radicals via spin trapping with BMPO. *J. Phys. Chem. A* **128**, 10240–10249 (2024).

42. P. Ausloos, The photolysis of alkyl esters. *Can. J. Chem.* **36**, 383–392 (1958).

43. J. K. Royal, G. K. Rollefson, The photolysis of simple alkyl esters. *J. Am. Chem. Soc.* **63**, 1521–1525 (1941).

44. E. Bothe, M. N. Schuchmann, D. Schulte-Frohlinde, C. V. Sonntag, HO_2 elimination from α-hydroxyalkylperoxyl radicals in aqueous solution. *Photochem. Photobiol.* **28**, 639–643 (1978).

45. W. H. Park, A comprehensive review of pyrogallol: From fundamental chemistry to advanced applications and toxicological insights. *Biotech. Bioeng.* **123**, 527–543, (2025).

46. Z. Fang, A. Lai, D. Cai, R. Chunlin Li, J. Carmieli, X. Chen, Y. R. Wang, Secondary organic aerosol generated from biomass burning emitted phenolic compounds: Oxidative potential, reactive oxygen species, and cytotoxicity. *Environ. Sci. Technol.* **58**, 8194–8206 (2024).

47. H. Tong, P. S. J. Lakey, A. M. Arangio, J. Socorro, F. Shen, K. Lucas, W. H. Brune, U. Pöschl, M. Shiraiwa, Reactive oxygen species formed by secondary organic aerosols in water and surrogate lung fluid. *Environ. Sci. Technol.* **52**, 11642–11651 (2018).

48. C. Arellanes, S. E. Paulson, P. M. Fine, C. Sioutas, Exceeding of Henry's law by hydrogen peroxide associated with urban aerosols. *Environ. Sci. Technol.* **40**, 4859–4866 (2006).

49. K. McNeill, S. Canonica, Triplet state dissolved organic matter in aquatic photochemistry: Reaction mechanisms, substrate scope, and photophysical properties. *Environ. Sci. Processes Impacts* **18**, 1381–1399 (2016).

50. Y. Zhang, R. Del Vecchio, N. V. Blough, Investigating the mechanism of hydrogen peroxide photoproduction by humic substances. *Environ. Sci. Technol.* **46**, 11836–11843 (2012).

51. D. J. Lary, D. E. Shallcross, Central role of carbonyl compounds in atmospheric chemistry. *J. Geophys. Res.* **105**, 19771–19778 (2000).

52. T. Berkemeier, M. Ammann, U. K. Krieger, T. Peter, P. Spichtinger, U. Pöschl, M. Shiraiwa, A. J. Huisman, Technical note: Monte Carlo genetic algorithm (MCGA) for model analysis of multiphase chemical kinetics to determine transport and reaction rate coefficients using multiple experimental data sets. *Atmos. Chem. Phys.* **17**, 8021–8029 (2017).

53. H. Sakugawa, I. R. Kaplan, W. Tsai, Y. Cohen, Atmospheric hydrogen peroxide. *Environ. Sci. Technol.* **24**, 1452–1462 (1990).

54. M. Fujii, E. Otani, Photochemical generation and decay kinetics of superoxide and hydrogen peroxide in the presence of standard humic and fulvic acids. *Water Res.* **123**, 642–654 (2017).

55. T. Arakaki, C. Anastasio, Y. Kuroki, H. Nakajima, K. Okada, Y. Kotani, D. Handa, S. Azechi, T. Kimura, A. Tsuhako, Y. Miyagi, A general scavenging rate constant for reaction of hydroxyl radical with organic carbon in atmospheric waters. *Environ. Sci. Technol.* **47**, 8196–8203 (2013).

56. M. C. Barth, B. Ervens, H. Herrmann, A. Tilgner, V. F. McNeill, W. G. Tsui, L. Deguillaume, N. Chaumerliac, A. Carlton, S. M. Lance, Box model intercomparison of cloud chemistry. *J. Geophys. Res. Atmos.* **126**, 10.1029/2021JD035486 (2021).

57. L. Ma, R. Worland, W. Jiang, C. Niedek, C. Guzman, K. J. Bein, Q. Zhang, C. Anastasio, Predicting photooxidant concentrations in aerosol liquid water based on laboratory extracts of ambient particles. *Atmos. Chem. Phys.* **23**, 8805–8821 (2023).

58. C. Anastasio, B. C. Faust, J. M. Allen, Aqueous phase photochemical formation of hydrogen peroxide in authentic cloud waters. *J. Geophys. Res.* **99**, 8231–8248 (1994).

59. M. O. Sunday, L. M. Dahler Heinlein, J. He, A. Moon, S. Kapur, T. Fang, K. C. Edwards, F. Guo, J. Dibb, J. H. Flynn Iii, B. Alexander, M. Shiraiwa, C. Anastasio, Hydrogen peroxide photoformation in particulate matter and its contribution to S(IV) oxidation during winter in Fairbanks, Alaska. *Atmos. Chem. Phys.* **25**, 5087–5100 (2025).

60. R. Kaur, C. Anastasio, Light absorption and the photoformation of hydroxyl radical and singlet oxygen in fog waters. *Atmos. Environ.* **164**, 387–397 (2017).

61. F. Leresche, J. R. Salazar, D. J. Pfotenhauer, M. P. Hannigan, B. J. Majestic, F. L. Rosario-Ortiz, Photochemical aging of atmospheric particulate matter in the aqueous phase. *Environ. Sci. Technol.* **55**, 13152–13163 (2021).

62. S. M. Griffith, R. F. Hansen, S. Dusanter, V. Michoud, J. B. Gilman, W. C. Kuster, P. R. Veres, M. Graus, J. A. De Gouw, J. Roberts, C. Young, R. Washenfelder, S. S. Brown, R. Thalman, E. Waxman, R. Volkamer, C. Tsai, J. Stutz, J. H. Flynn, N. Grossberg, B. Lefer, S. L. Alvarez, B. Rappenglueck, L. H. Mielke, H. D. Osthoff, P. S. Stevens, Measurements of hydroxyl and hydroperoxy radicals during CalNex-LA: Model comparisons and radical budgets. *J. Geophys. Res. Atmos.* **121**, 4211–4232 (2016).

63. P. Liu, C. Ye, C. Zhang, G. He, C. Xue, J. Liu, C. Liu, Y. Zhang, Y. Song, X. Li, X. Wang, J. Chen, H. He, H. Herrmann, Y. Mu, Photochemical aging of atmospheric fine particles as a potential source for gas-phase hydrogen peroxide. *Environ. Sci. Technol.* **55**, 15063–15071 (2021).

64. H. A. Al-Abadleh, S. A. Nizkorodov, Open questions on transition metals driving secondary thermal processes in atmospheric aerosols. *Commun. Chem.* **4**, 176 (2021).

65. L. M. D. Heinlein, J. He, M. O. Sunday, F. Guo, J. Campbell, A. Moon, S. Kapur, T. Fang, K. Edwards, M. Cesler-Maloney, A. J. Burns, J. Dibb, W. Simpson, M. Shiraiwa, B. Alexander, J. Mao, J. H. Flynn III, J. Stutz, C. Anastasio, Surprisingly robust photochemistry in subarctic particles during winter: Evidence from photooxidants. *Atmos. Chem. Phys.* **25**, 9561–9581 (2025).

66. W. Jiang, C. Niedek, C. Anastasio, Q. Zhang, Photoaging of phenolic secondary organic aerosol in the aqueous phase: Evolution of chemical and optical properties and effects of oxidants. *Atmos. Chem. Phys.* **23**, 7103–7120 (2023).

67. Z. Liang, L. Zhou, Y. Chang, Y. Qin, C. K. Chan, Biomass-burning organic aerosols as a pool of atmospheric reactive triplets to drive multiphase sulfate formation. *Proc. Natl. Acad. Sci. U.S.A.* **121**, e2416803121 (2024).

68. E. Harris, B. Sinha, D. Van Pinxteren, A. Tilgner, K. W. Fomba, J. Schneider, A. Roth, T. Gnauk, B. Fahlbusch, S. Mertes, T. Lee, J. Collett, S. Foley, S. Borrmann, P. Hoppe, H. Herrmann, Enhanced role of transition metal ion catalysis during in-cloud oxidation of SO_2. *Science* **340**, 727–730 (2013).

69. Y. Yan, T. Zhao, W. Huang, D. Fang, X. Zhang, L. Zhang, P. Huo, K. Xiao, Y. Zhang, Y. Zhang, The complexation between transition metals and water-soluble organic compounds (WSOC) and its effect on reactive oxygen species (ROS) formation. *Atmos. Environ.* **287**, 119247 (2022).

70. T. Finkel, N. J. Holbrook, Oxidants, oxidative stress and the biology of ageing. *Nature* **408**, 239–247 (2000).

71. J. P. S. Wong, M. Tsagkaraki, I. Tsiodra, N. Mihalopoulos, K. Violaki, M. Kanakidou, J. Sciare, A. Nenes, R. J. Weber, Effects of atmospheric processing on the oxidative potential of biomass burning organic aerosols. *Environ. Sci. Technol.* **53**, 6747–6756 (2019).

72. P. H. Chowdhury, Q. He, T. Lasitza Male, W. H. Brune, Y. Rudich, M. Pardo, Exposure of lung epithelial cells to photochemically aged secondary organic aerosol shows increased toxic effects. *Environ. Sci. Technol. Lett.* **5**, 424–430 (2018).

73. L. Gerritz, M. Schervish, P. S. J. Lakey, T. Oeij, J. Wei, S. A. Nizkorodov, M. Shiraiwa, Photoenhanced radical formation in aqueous mixtures of levoglucosan and benzoquinone: Implications to photochemical aging of biomass-burning organic aerosols. *J. Phys. Chem. A* **127**, 5209–5221 (2023).

74. R. Schmid, S. Heuckeroth, A. Korf, A. Smirnov, O. Myers, T. S. Dyrlund, R. Bushuiev, K. J. Murray, N. Hoffmann, M. Lu, A. Sarvepalli, Z. Zhang, M. Fleischauer, K. Dührkop, M. Wesner, S. J. Hoogstra, E. Rudt, O. Mokshyna, C. Brungs, K. Ponomarov, L. Mutabdžija, T. Damiani, C. J. Pudney, M. Earll, P. O. Helmer, T. R. Fallon, T. Schulze, A. Rivas-Ubach, A. Bilbao, H.

Richter, L.-F. Nothias, M. Wang, M. Orešič, J.-K. Weng, S. Böcker, A. Jeibmann, H. Hayen, U. Karst, P. C. Dorrestein, D. Petras, X. Du, T. Pluskal, Integrative analysis of multimodal mass spectrometry data in MZmine 3. *Nat. Biotechnol.* **41**, 447–449 (2023).

75. J. Wei, T. Fang, P. S. J. Lakey, M. Shiraiwa, Iron-facilitated organic radical formation from secondary organic aerosols in surrogate lung fluid. *Environ. Sci. Technol.* **56**, 7234–7243 (2022).

76. R. Sander, Compilation of Henry's law constants (version 5.0.0) for water as solvent. *Atmos. Chem. Phys.* **23**, 10901–12440 (2023).

77. I. V. Perminova, F. H. Frimmel, A. V. Kudryavtsev, N. A. Kulikova, G. Abbt-Braun, S. Hesse, V. S. Petrosyan, Molecular weight characteristics of humic substances from different environments as determined by size exclusion chromatography and their statistical evaluation. *Environ. Sci. Technol.* **37**, 2477–2485 (2003).

78. D. K. Banerjee, C. C. Budke, Spectrophotometric determination of traces of peroxides in organic solvents. *Anal. Chem.* **36**, 792–796 (1964).

79. H. Keller-Rudek, G. K. Moortgat, R. Sander, R. Sörensen, The MPI-Mainz UV/VIS Spectral Atlas of gaseous molecules of atmospheric interest. *Earth Syst. Sci. Data* **5**, 365–373 (2013).

80. N. F. Christensen, R. Odai, K. H. Bates, H. G. Kjaergaard, Calculated absorption cross sections and photolysis rates of hydroperoxyaldehydes. *J. Phys. Chem. A* **130**, 111–120 (2026).

81. S. Hsieh, R. Vushe, Y. T. Tun, J. L. Vallejo, Trends in organic hydroperoxide photodissociation and absorption cross sections between 266 and 377 nm. *Chem. Phys. Lett.* **591**, 99–102 (2014).

82. H. Jiang, C. M. S. Ahmed, Z. Zhao, J. Y. Chen, H. Zhang, A. Canchola, Y.-H. Lin, Role of functional groups in reaction kinetics of dithiothreitol with secondary organic aerosols. *Environ. Pollut.* **263**, 114402 (2020).

83. R. Atkinson, J. Arey, Atmospheric degradation of volatile organic compounds. *Chem. Rev.* **103**, 4605–4638 (2003).

84. P. B. Shepson, E. O. Edney, E. W. Corse, Ring fragmentation reactions in the photooxidations of toluene and o-xylene. *J. Phys. Chem.* **88**, 4122–4126 (1984).

85. O. Garmash, M. P. Rissanen, I. Pullinen, S. Schmitt, O. Kausiala, R. Tillmann, D. Zhao, C. Percival, T. J. Bannan, M. Priestley, Å. M. Hallquist, E. Kleist, A. Kiendler-Scharr, M. Hallquist, T. Berndt, G. McFiggans, J. Wildt, T. F. Mentel, M. Ehn, Multi-generation OH oxidation as a source for highly oxygenated organic molecules from aromatics. *Atmos. Chem. Phys.* **20**, 515–537 (2020).

86. J. H. Seinfeld, S. N. Pandis, *Atmospheric Chemistry and Physics: From Air Pollution to Climate Change*, New York Academy of Sciences Series (John Wiley & Sons Inc., ed. 1, 2016).

87. M. Shiraiwa, U. Pöschl, Mass accommodation and gas–particle partitioning in secondary organic aerosols: Dependence on diffusivity, volatility, particle-phase reactions, and penetration depth. *Atmos. Chem. Phys.* **21**, 1565–1580 (2021).

88. B. Aumont, S. Szopa, S. Madronich, Modelling the evolution of organic carbon during its gas-phase tropospheric oxidation: Development of an explicit model based on a self generating approach. *Atmos. Chem. Phys.* **5**, 2497–2517 (2005).